ISSN 0030-400X, Optics and Spectroscopy, 2014, Vol. 116, No. 5, pp. 715–720. © Pleiades Publishing, Ltd., 2014.
Original Russian Text © T.B. Biktagirov, M.R. Gafurov, G.V. Mamin, S.B. Orlinskii, B.V. Yavkin, A.A. Rodionov, E.S. Klimashina, V.I. Putlyaev, Ya.Yu. Fillipov, 2014, published in Optika i Spektroskopiya, 2014, Vol. 116, No. 5, pp. 774–780.

XV INTERNATIONAL FEOFILOV SYMPOSIUM

A Study of Hydroxyapatite Nanocrystals by the Multifrequency EPR and ENDOR Spectroscopy Methods

T. B. Biktagirov[a], M. R. Gafurov[a], G. V. Mamin[a], S. B. Orlinskii[a], B. V. Yavkin[a], A. A. Rodionov[a], E. S. Klimashina[b], V. I. Putlyaev[b], and Ya. Yu. Fillipov[b]

[a] *Institute of Physics, Kazan (Volga Region) Federal University, Kazan, Tatarstan, 420008 Russia*

[b] *Faculty of Materials Science, Moscow State University, Moscow, 119991 Russia*

e-mail: tbiktagirov@gmail.com

Received November 18, 2013

Abstract—Specimens of powders of hydroxyapatite ($Ca_{10}(PO_4)_6(OH)_2$) with average crystallite sizes in the range of 20–50 nm synthesized by the wet precipitation method have been investigated by the multifrequency (9 and 94 GHz) electron paramagnetic resonance (EPR) and electron–nuclear double resonance (ENDOR) methods. In specimens subjected to X-ray irradiation at room temperature, EPR signals that are caused by nitrogen compounds have been observed. Numerical calculations performed in terms of the density functional theory show that the observed EPR signal is caused by the occurrence of paramagnetic centers, the structure of which is NO_3^{2-} and which replace the positions of PO_4^{3-} in the hydroxyapatite structure.

DOI: 10.1134/S0030400X14050051

INTRODUCTION

Over the last decade, interest in materials based on hydroxyapatite ($Ca_{10}(PO_4)_6(OH)_2$) has increased [1–3]. Modified hydroxyapatite possesses a wide spectrum of both potential and realized applications not only in instrumentation technology (sorbents, luminophores, piezoelectrics), but also for biomedical applications (materials for implantation of bone tissue, for targeted delivery of fluorescent preparations, contrast agents, and drugs to tissues under investigation, sorbents of heavy metals, etc.). Modern biomedical applications are putting increased demands on the individual and general biocompatibility of materials based on hydroxyapatite. In view of the tendency to move to nanosized objects, this unavoidably leads to the necessity of application of various types of analytical equipment for comprehensive investigation of new synthetic materials, controlling their quality, monitoring of changes in their physicochemical characteristics in the course of time or under the action of various external factors (temperature, humidity, acidity, chemical action, etc.). EPR and electron–nuclear double resonance (ENDOR) spectroscopy are efficient methods of identification of natural or artificially created paramagnetic defects, determination of their structure, and localization (see recent review [4] and works [5–7]). However, for various reasons, these methods are still usually not considered some of the standard techniques that are used for thorough analysis of materials based on hydroxyapatite [8].

In order to study natural (biogenic) hydroxyapatites, centers that arise under the action of ionizing radiation are used as paramagnetic probes. In irradiated specimens, the EPR and ENDOR methods made it possible to identify a considerable number of inorganic radicals, such as O^-, O_3^-, CO_3^-, CO_3^{3-}, CO_2^-, CO, PO_4^-, and H^0 [4]. From the viewpoint of practical applications, CO_2^- radicals, which are highly stable, are of great interest. They can be localized either in the positions of OH (A-type substitution) or in the positions of PO_4 (B-type substitution). EPR spectra of CO_2^- radicals, in addition to being useful for dosimetric purposes, can be used to characterize the degree of calcification of vessel walls in the case of atherosclerosis [5].

This work is devoted to the investigation of powders of hydroxyapatite nanocrystals (with an average size of nanocrystallites of 20–50 nm) by the EPR and ENDOR methods. One of the objectives of this investigation was to show possibilities and restrictions of the used experimental and calculational techniques for studying hydroxyapatites and compositions based on them, which will make it possible to extend the range of applications of magnetic resonance methods in this field.

MATERIALS AND METHODS

Hydroxyapatite powders were synthesized by the aqueous precipitation method. To this end, we used chemically pure aqueous solutions of $Ca(NO_3)_2$, $(NH_4)_2HPO_4$, and NH_4OH in stoichiometric proportions. Obtained specimens were characterized by the

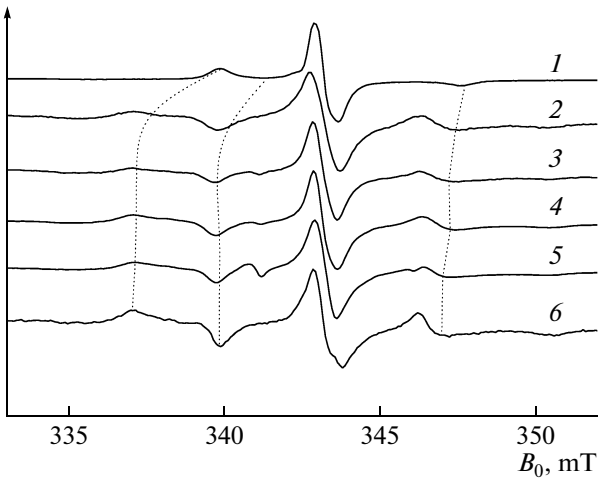

Fig. 1. EPR spectra of annealed hydroxyapatite nanocrystals (20 nm) detected in the continuous wave regime in X-band at $T = 300$ K. Annealing temperature: (*1*) 500, (*2*) 450, (*3*) 400, (*4*) 350, (*5*) 250, and (*6*) 25°C.

methods of transmission electron microscopy (LEO Sopra 50VP, Carl Zeiss, 5 kV), X-ray phase analysis (Rigaku D/MAX 2500 with rotating anode and Bruker D2 Phaser), local X-ray microanalysis (INCA Energy+ combined with LEO Supra 50VP), and infrared spectroscopy (PerkinElmer 1600). Synthesis of materials and laboratory analysis thereof were performed at the Faculty of Materials Science of Moscow State University. Details of the synthesis and of the chemical and thermal processing aimed at achieving a maximal degree of crystallinity and degree of purification of the final product from extraneous impurities were presented in [6, 9].

Using EPR methods, we studied specimens with an average size of crystallites of 20–50 nm. No EPR signals from examined specimens were observed. To create paramagnetic complexes, specimens under study were irradiated with X rays at room temperature using a URS-55 setup ($U = 55$ kV, $I = 16$ mA, W anticathode), irradiation dose was about 5–10 kGy. To investigate the EPR/ENDOR spectra, we used a spectrometer from the Center of Collective Usage for Physicochemical Research at Kazan Federal University. The instrument was an Elexsys 580/680 combined spectrometer (Bruker), which can operate in a continuous or pulsed regime either at the X-band (9 GHz) or at the high-frequency W-band (94 GHz). In the pulsed regime, standard two- or three-pulse sequences were used [10]. Measurements were performed at temperatures of 50 and 300 K. Specimens were studied prior to and after X ray irradiation.

Quantum-chemical investigation of the structure of impurity centers and calculations of their total energy were performed in terms of the density functional theory (DFT) using a Perdew–Burke–Ernzerhof generalized gradient approximation [11] for the exchange–correlation functional and Vanderbilt ultrasoft pseudopotentials [12]. Calculations were performed using the Quantum Espresso package [13] in terms of computational capabilities provided by the Institute of Physics of Kazan Federal University. To test pseudopotentials, we performed preliminary calculations for a cell of stoichiometric hydroxyapatite. Based on the results of convergence of the total energy, the cutoff value of the kinetic energy of plane waves was chosen to be 40 Ry.

Impurity incorporation energies were obtained with preliminary optimization of the positions of all atoms in the supercell and the lattice constants. The structure was optimized using the Broyden–Fletcher–Goldfarb–Shanno algorithm. The supercell was constructed based on the monoclinic modification of hydroxyapatite (the $P2_1/b$ symmetry group) [14]. In the work, we used the supercells of two sizes, which contained 88 and, for the stoichiometric crystal, 176 atoms.

In order to investigate the properties of the NO_3^{2-} paramagnetic center, calculations were performed in the spin-polarized formalism introducing an additional electron into the cell. Constants of the hyperfine interaction and components of the g tensor were calculated using the gauge-including projector augmented wave (GIPAW) approach [15].

EXPERIMENTAL RESULTS

All examined specimens exhibited EPR signals after their X-ray irradiation in the continuous regime. Figure 1 shows the EPR spectrum in the range of the X-band at $T = 300$ K and its changes after specimens exposed to the action of the ionizing radiation were annealed at different temperatures for 4 h under the conditions of a deep vacuum ($<10^{-4}$ mbar). The annealing temperature had no effect on the integrated intensity of the observed signal. The concentration of paramagnetic impurities was estimated from comparison with the reference signal from Mn^{2+} ions in a powder of a MgO crystal and was determined to be $5(1) \times 10^{18}$ spin/g.

Figure 2 presents EPR spectra of a specimen with a particle size of 20 nm prior to its annealing, which were recorded in the pulsed regime at $T = 300$ K. The powder EPR spectrum that we observed in the range of the X-band (Fig. 2a) differs from the spectra of inorganic radicals, which are typical for biogenic hydroxyapatite and which were described above, and it is likely that it is caused by the occurrence of NO_3^{2-} or NO_2^{2-} nitrogen-centered radicals, which have close spectroscopic parameters [16–21]. The spectrum was simulated best under the assumption of the observation of axially symmetric nitrogen-centered radicals, the parameters of which are presented in Table 1. The occurrence of a nuclear spin $I = 1$ in the nitrogen iso-

tope ^{14}N determines the observation of three lines as a result of the hyperfine interaction of the nitrogen nucleus with electron spin $S = 1/2$. Clearly, changes in the EPR spectrum that are observed upon annealing are primarily determined precisely by changes in the parameters of the hyperfine structure. Remarkably, the values of temperatures at which this effect is observed are considerably lower than the temperature of the phase transition hydroxyapatite–tricalcium phosphate but higher than the temperature of evaporation of water molecules that are absorbed by hydroxyapatite [22].

A high stability of this paramagnetic center and long relaxation times, which make it possible to observe the EPR spectrum in the pulsed regime at room temperature, allow us to assume that, in our measurements, with a high probability, we observe the spectrum of stable NO_3^{2-} radicals. Taking into account the fact that the concentration of NO_3^{2-} radicals that we determine does not depend on the size of crystallites, based on the experimental results presented above, we can with certainty assume that the observed paramagnetic centers are incorporated into the crystal lattice of hydroxyapatite. It is important to emphasize that, from the practical point of view, the occurrence of the nitrogen-containing impurity in the structure of hydroxyapatite is an undesirable factor [20]. It should also be noted that we failed to detect nitrogen-containing compounds in examined specimens neither prior to nor after their X-ray irradiation using both the IR spectroscopy technique and the X-ray fluorescence analysis. The fact of the absence of NO_3 vibrational modes in IR spectra still has not been adequately explained in the literature [9, 23].

Figure 2b presents the EPR spectrum at $T = 300$ K in W-band and the result of its simulation with parameters given in Table 1. Due to a higher sensitivity and better spectral resolution at a high frequency, apart from the EPR signal from nitrogen-centered radicals, additional lines are observed, which we attribute to CO_2^- carbonate ions (cf. work [5]). To refine the localization of the observed nitrogen-centered radical, we performed investigations by the ENDOR method. Due to the spectral and quasi-orientational resolution of EPR spectra in W-band, we selected the value of the induction B_0 of the external magnetic field such that the observed spectrum would be contributed predominantly by radicals with a perpendicular component of the g tensor, which is oriented along the direction of $\mathbf{B}_0$ (perpendicular orientation, Fig. 2b). ENDOR spectra at $T = 50$ K and values of frequencies that correspond to the Larmor frequencies of the ^1H and ^{31}P nuclei are presented in Fig. 3. It should be noted that, at room temperature, the ENDOR spectra were also observed; however, the signal-to-noise ratio was considerably worse in this case and did not allow us to observe all

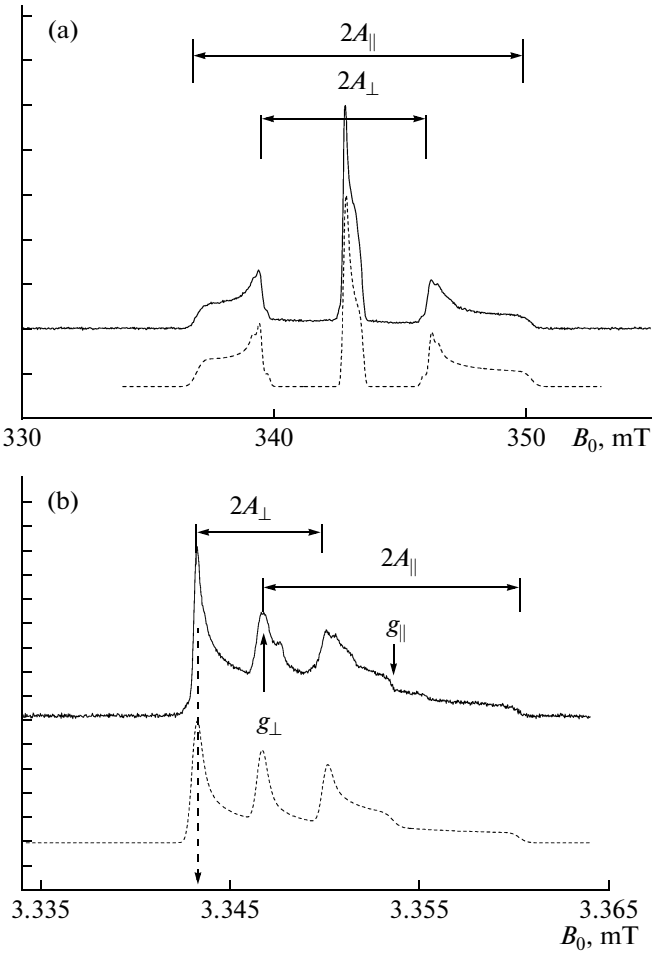

Fig. 2. Experimental (solid curves) and simulated (dashed curves; simulation parameters are given in Table 1) EPR spectra of NO_3^{2-} in hydroxyapatite nanocrystals that were obtained upon detection of the electron spin echo amplitude: (a) X-band, $T = 300$ K; (b): W-band, $T = 50$ K. The vertical dashed arrow indicates the value of B_0 at which the ENDOR spectra were investigated.

Table 1. Experimental and DFT calculated parameters of EPR spectra of NO_3^{2-} radiation centers in the hydroxyapatite structure; for comparison with experimental data: $(g, A)_{||} = (g, A)_{zz}$, $(g, A)_{\perp} = [(g, A)_{xx} + (g, A)_{yy}]/2$

	g_{xx}	g_{yy}	g_{zz}	A_{xx}, mT	A_{yy}, mT	A_{zz}, mT
Experiment	2.0055(5)	2.0055(5)	2.0015(5)	3.35(40)	3.35(40)	6.65(40)
Calculation	2.00616	2.00652	2.00158	3.277	3.273	6.413

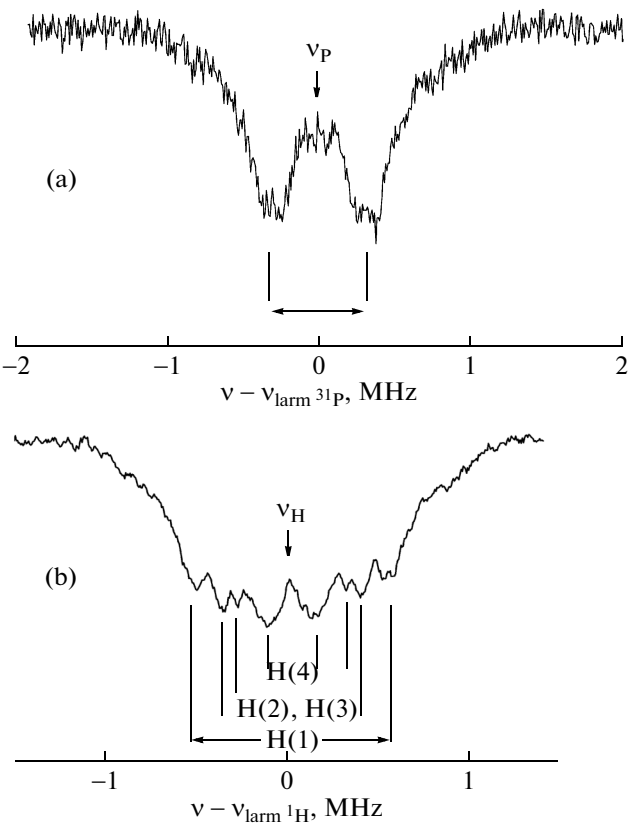

Fig. 3. ENDOR spectra of hydroxyapatite nanocrystals (30 nm) in the range of the W-band at $T = 50$ K: (a) the range of the Larmor frequency of phosphorus ^{31}P; (b) the range of the Larmor frequency of protons ^{1}H.

splittings that manifest themselves at low temperatures. We failed to detect the ENDOR spectrum of nitrogen nuclei, which, based on the EPR data, should be distributed in the frequency range of 95–186 MHz, which, in turn, leads to an extremely low peak intensity of the ENDOR signal.

From the ENDOR spectrum, we can single out the strongest hyperfine interactions with one phosphorus ion and four hydrogen ions. Results of measurements of ENDOR spectra and distances to the nearest ligands estimated in the approximation that takes into account only magnetic dipole–dipole interaction [6] are presented in Table 2. Analyzing the data on the crystallographic structure of hydroxyapatite and comparing interatomic distances for different positions in the structure of hydroxyapatite and phosphorus and hydrogen ions nearest to them [24], we can assume that there are two types of the substitution that are most probable for nitrate ions, which we, similarly to the case of incorporation of carbonate ions, will denote as A- and B-type substitutions, respectively (Table 2). In order to refine the localization of the NO_3^{2-} radical and to explain changes in the experimentally observed constants of the hyperfine interaction with ^{14}N nuclei upon annealing (Fig. 1), we performed numerical calculations in terms of the DFT method.

NUMERICAL DFT-CALCULATIONS

Based on the analysis of ENDOR spectra, we considered two possible models of the structure of hydroxyapatite that contains a NO_3^- impurity. In one case, the structure has the A-type substitution, while, in the other one, this is substitution of the B type. For the case of the substitution of the PO_4^{3-} group with nitrate (B type), we considered the charge compensation scheme in which one of Ca^{2+} ions neighboring to nitrate is removed.

For either of the investigated configurations, we performed several independent cycles of optimization of the geometry with different initial conditions. In both cases, the impurity nitrate has the same planar configuration with an average length of the N–O bond, equal to 0.13 nm. For the localization in the ON channel, the plane of the nitrate makes an angle with the crystallographic *b* axis, which is approximately equal to 153°; for the position of PO_4, the nitrate is almost perpendicular to the *b* axis (the inclination

Table 2. Experimental values of splittings in the ENDOR spectrum, values of electron–nucleus distances calculated from experiment in the dipole–dipole approximation (r_{exp}), and comparison with the data from the literature for two probable positions of substitution with nitrogen-centered radicals (r_{calc})

Nucleus	Splitting in the ENDOR spectrum, MHz	r_{exp}, nm	r_{calc} in the position of OH, nm	r_{calc} in the position of PO_4^{3-}, nm
H(1)	1.06(1)	0.42(1)	0.32	0.48
H(2)	0.75(1)	0.47(1)	0.37	0.5
H(3)	0.60(1)	0.51(1)	0.66	0.67
H(4)	0.26(1)	0.67(1)	0.71	0.71
P	0.64 (6)	0.37(1)	0.40	0.32
$\Sigma(r_{exp} - r_{calc})^2$, nm^2			0.045	0.034

Table 3. Lattice constants of hydroxyapatite calculated for the stoichiometric and nitrate-substituted unit cells; comparison with the data from the literature

Lattice type		a, nm	b, nm	c, nm
Stoichiometric hydroxyapatite	[24, 25]	0.942	0.688	1.885
	calculation	0.949	0.691	1.896
NO_3^--containing hydroxyapatite	A type, calculation	0.957	0.689	1.921
	B type, calculation	0.947	0.690	1.903

angle is 79°). As expected, the introduction of the nitrate causes significant structural deformations. However, the parameters of the lattice that were obtained for the two considered models are close to those that are characteristic of stoichiometric hydroxyapatite (Table 3).

In order to compare the probabilities of realization of either of the considered models of substitution, we calculated the energies of formation of defects using the following formulas:

$$E_{\text{form}}(\text{A-NO}_3) = E(\text{A-NO}_3) - E(\text{HAp}) - \mu_N - 2\mu_O + \mu_H, \quad (1)$$

$$E_{\text{form}}(\text{B-NO}_3) = E(\text{B-NO}_3) - E(\text{HAp}) - \mu_N + \mu_{Ca} + \mu_P + \mu_O. \quad (2)$$

Here, E(HAp), E(A-NO_3), and E(B-NO_3) are the total energies of the unit cell of stoichiometric hydroxyapatite and of the unit cells that contain the impurity NO_3^- ion in the position of the OH group and of the PO_4 group, respectively; μ_N is the chemical potential of the nitrogen atom, which, in this work, was taken to be half of the energy of the N_2 molecule. The chemical potentials of the Ca (μ_{Ca}), P (μ_P), O (μ_O), and H (μ_H) atoms satisfy the following condition of the thermodynamic equilibrium:

$$10\mu_{Ca} + 6\mu_P + 2\mu_H + 26\mu_O = \mu_{HAp} \quad (3)$$

and, in the general case, depend on experimental conditions of the crystal growth; determining their values is attended with a certain ambiguity. It is also assumed that the value of μ_{HAp} at zero temperature and zero pressure is equal to the value of E(HAp). In practice, chemical potentials of atoms can be set for an appropriate reference system [25]. In this work, we considered two reference systems. In one case, the value of μ_{Ca} was determined by the calculated energy of the crystal form of calcium, while the values of μ_O and μ_H were determined by the energies of the O_2 and H_2 molecules, respectively. The obtained values of the formation energies E_{form}(A-NO_3) = 0.4 eV and E_{form}(B-NO_3) = −7.3 eV indicate that the B-type configuration is energetically more favorable. Qualitatively, a similar result was obtained for the second reference system (O_2, H_2, and phosphorus pentoxide (P_2O_5)): E_{form}(A-NO_3) = 0.4 eV and E_{form}(B-NO_3) = −1.3 eV. These results testify to the predominance of the B-type configuration (the position of the PO_4 group) in a wide range of experimental conditions. Remarkably, the calculated values of spectroscopic parameters of the corresponding paramagnetic center (NO_3^{2-}) agree well with experiment, which is shown in Table 1. Schematically, the structure of the paramagnetic defect "NO_3^{2-}–Ca vacancy" is shown in Fig. 4.

Based on the results of our numerical calculations, the influence of the thermal annealing on the parameters of the hyperfine structure of the NO_3^{2-} radical can be explained as follows. We revealed that the local structure of the defect significantly affects the localization of the spin density on the nitrogen nucleus and, as a consequence, the values of components of the A tensor of the NO_3^{2-} radical. Thus, for B-type configurations of the defect with different positions of Ca vacancy and comparatively close energies of the ground state, calculated constants of the hyperfine interaction are considerably different. The model of the defect in which its energy is the lowest agrees best with experimental spectroscopic parameters, and one can expect that, in the ground state, precisely this configuration predominates. However, upon annealing, the local environment of the paramagnetic center can

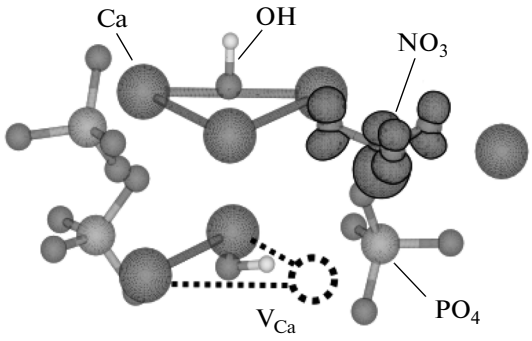

Fig. 4. Structure of a NO_3^{2-} paramagnetic defect in the B-type configuration that was obtained as a result of the geometry optimization. The circle denotes the position of the vacancy of calcium (V_{Ca}); the isosurface shows the distribution of the spin density.

become distorted (for instance, because of migration of the Ca vacancy), which leads to observed changes of spectroscopic parameters of the NO_3^{2-} center.

CONCLUSIONS

In this work, we have investigated specimens of nanocrystalline hydroxyapatite using EPR/ENDOR multifrequency spectroscopy methods. These methods have been shown to be efficient in establishing the nature and localization of nitrogen-containing impurity centers, which incorporate themselves into the structure of hydroxyapatite nanocrystals as undesirable impurities during the synthesis process. Although this impurity occurs in trace amounts in examined specimens, which did not allow one to detect it with other experimental techniques, a high sensitivity of the EPR methods yields the possibility of identifying stable NO_3^{2-} radiation centers.

In addition, we have shown that combining the experimental EPR spectroscopy methods with modern methods of quantum computations based on the density functional theory proves to be very informative, especially in cases in which the analysis of results of ENDOR measurement does not allow one to obtain an unambiguous pattern on the localization of impurity centers. A high degree of agreement between calculated and experimentally obtained spectroscopic parameters allows one to expect that the approach used in this work will prove to be highly efficient in studies of practically significant materials based on hydroxyapatite that are synthesized using more complicated (co)doping schemes.

REFERENCES

1. S. V. Dorozhkin, Am. J. Biomed. Eng. **2**, 48 (2012).
2. H. Zhou and J. Lee, Acta Biomat. **7**, 2769 (2011).
3. K. Hasna, S. Kumar, M. Komath, M. Varma, M. K. Jayaraj, and K. Kumar, Phys. Chem. Chem. Phys. **15**, 8106 (2013).
4. P. Fattibene and F. Callens, Appl. Radiat. Isotopes **68**, 2033 (2010).
5. V. A. Abdul'yanov, L. F. Galiullina, A. S. Galyavich, V. G. Izotov, G. V. Mamin, S. B. Orlinskii, A. A. Rodionov, M. Kh. Salakhov, N. I. Silkin, L. M. Sitdikova, R. N. Khairullin, and Yu. A. Chelyshev, Pis'ma Zh. Eksp. Teor. Fiz. **88** (1), 75 (2008).
6. B. V. Yavkin, G. V. Mamin, S. B. Orlinskii, M. R. Gafurov, M. Kh. Salakhov, T. B. Biktagirov, E. S. Klimashina, V. I. Putlayev, Yu. D. Tretyakov, and N. I. Silkin, Phys. Chem. Chem. Phys. **14**, 2246 (2012).
7. M. R. Gafurov, B. V. Yavkin, T. B. Biktagirov, et al., Magn. Reson. Sol. **15**, 13102 (2013).
8. M. Markovic, B. O. Fowler, and M. S. Tung, Material. J. Res. Nat. Inst. Stand. Technol. **109**, 553 (2004).
9. E. S. Kovaleva, M. P. Shabanov, V. I. Putlayev, Ya. Yu. Filippov, Y. D. Tretyakov, and V. K. Ivanov, Mat.–Wiss. Werkstofftec **39** (11), 822 (2008).
10. J. A. Weil and J. R. Bolton, *Electron Paramagnetic Resonance: Elementary Theory and Practical Applications*, 2nd ed. (Wiley, Hoboken, 2004).
11. J. P. Perdew, K. Burke, and M. Ernzerhof, Phys. Rev. Lett. **77** (18), 3865 (1996).
12. D. Vanderbilt, Phys. Rev. B **41** (11), 7892 (1990).
13. P. Giannozzi, J. Phys.: Con. Matter **21**, 395502 (2009).
14. M. Yashima, Y. Yonehara, and H. Fujimori, J. Phys. Chem. **115** (20), 25077 (2011).
15. C. J. Pickard and F. Mauri, Phys. Rev. B **63** (24), 245101 (2001).
16. R. S. Eachus and M. C. R. Symons, J. Chem. Soc. Am. 790 (1968).
17. S. I. Bannov and V. A. Nevostruev, Radiat. Phys. Chem. **68**, 917 (2003).
18. I. P. Vorona, S. S. Ishchenko, N. P. Baran, et al., Fiz. Tverd. Tela **52** (11), 2211 (2010).
19. N. P. Baran, I. P. Vorona, S. S. Ishchenko, et al., Fiz. Tverd. Tela **53** (9), 1791 (2011).
20. A. B. Brik, A. P. Shpak, A. P. Klimenko, et al., Miner. J. (Ukraine) **28**, 20 (2006).
21. J. Dugas, B. Bejjaji, D. Sayah, and J. C. Trombe, J. Solid State Chem. **24**, 143 (1978).
22. W. E. Lee and W. M. Rainforth, *Ceramic Microstructures: Property Control by Processing* (Chapman and Hall, 1994).
23. J. F. Stanton, J. Chem. Phys. **126**, 134309 (2007).
24. M. Yashima, Y. Yonehara, and H. Fujimori, J. Phys. Chem. **115**, 25077 (2011).
25. C. G. Van de Walle and J. Neugebauer, J. Appl. Phys. **95** (8), 3851 (2004).

Translated by V. Rogovoi